Journal of Physics D: Applied Physics

PAPER

Anisotropic deformation of 4H-SiC wafers: insights from nanoindentation tests

To cite this article: Xiaoshuang Liu *et al* 2022 *J. Phys. D: Appl. Phys.* **55** 494001

IOP Publishing Journal of Physics D: Applied Physics

J. Phys. D: Appl. Phys. **55** (2022) 494001 (8pp) https://doi.org/10.1088/1361-6463/ac9535

Anisotropic deformation of 4H-SiC wafers: insights from nanoindentation tests

Xiaoshuang Liu[1,2,3], **Rong Wang**[2,3,*], **Junran Zhang**[1,2,3], **Yunhao Lu**[1,2], **Yiqiang Zhang**[4], **Deren Yang**[2,3] **and Xiaodong Pi**[2,3,*]

[1] Zhejiang Province Key Laboratory of Quantum Technology and Device, Department of Physics, Zhejiang University, Hangzhou 310027, People's Republic of China
[2] State Key Laboratory of Silicon Materials & School of Materials Science and Engineering, Zhejiang University, Hangzhou, Zhejiang 310027, People's Republic of China
[3] Institute of Advanced Semiconductors & Zhejiang Provincial Key Laboratory of Power Semiconductor Materials and Devices, Hangzhou Innovation Center, Zhejiang University, Hangzhou, Zhejiang 311200, People's Republic of China
[4] School of Materials Science and Engineering & Henan Institute of Advanced Technology, Zhengzhou University, Zhengzhou, Henan 450001, People's Republic of China

E-mail: rong_wang@zju.edu.cn and xdpi@zju.edu.cn

Received 16 June 2022, revised 6 September 2022
Accepted for publication 27 September 2022
Published 27 October 2022

Abstract

In this work, the anisotropic deformation and anisotropic mechanical properties of 4H silicon carbide (4H-SiC) single crystal wafers are proposed by using nanoindentation. The C face of a 4H-SiC wafer has higher hardness and lower fracture toughness than those of the Si face. Because the deformation of 4H-SiC is assisted by the nucleation and slip of basal plane dislocations (BPDs), especially the slip of Si-core partial dislocations (PDs) of the BPDs, the nucleation and slip of the Si-core PDs in the Si face of 4H-SiC is easier than those in the C face, which releases the nanoindentation-induced stress and results in the decrease of the hardness and increase of the fracture toughness of the Si face of 4H-SiC wafers. Due to the hexagonal lattice of 4H-SiC, the hardness along $< 1\bar{1}00 >$ of 4H-SiC is higher than that along $< 11\bar{2}0 >$, but the fracture toughness along the $< 1\bar{1}00 >$ is lower than that along the $< 11\bar{2}0 >$, as a result of the enhanced glide of dislocations along the most closely-packed direction. The insights gained in this work are expected to shed light on the optimization of the mechanical processing of 4H-SiC wafers.

Keywords: 4H-SiC, wafer, dislocations, mechanical properties, anisotropic deformation

(Some figures may appear in colour only in the online journal)

1. Introduction

With the explosive development of high-power and high frequency electronics, 4H silicon carbide (4H-SiC) wafers have attracted great interests owing to its wide bandgap, high breakdown electric field, high electron saturation mobility, high thermal conductivity and strong radiation resistance [1–5]. From physical vapor transport-grown 4H-SiC boules, the processing of 4H-SiC wafers includes wire slicing, lapping, and chemical mechanical polishing (CMP) [6]. Due to the high hardness and high brittleness of 4H-SiC, the high-density processing damages, low processing efficiency and high processing costs are long-standing problems in the

* Authors to whom any correspondence should be addressed.

mechanical processing of 4H-SiC wafers [7]. It has been found that processing-induced dislocations and subsurface damages significantly degrades the quality of 4H-SiC based epitaxial layers and thus the performance of 4H-SiC devices [8]. Reducing the processing-induced damages by optimizing the processing steps is one of the most challenging issues for the mechanical processing of 4H-SiC wafers. During the lapping and CMP of 4H-SiC wafers, the C face exhibits higher removal rate and lower roughness than those of the Si face of 4H-SiC wafers [9, 10]. This indicates that deformation mechanisms of the Si face and C face of 4H-SiC wafers are different during the mechanical processing. Given the hexagonal lattice of 4H-SiC, the preferential removal along the $< 11\bar{2}0 >$ has been found, though the anisotropic deformation mechanism is still ambiguous. Based on thorough understanding on the anisotropic deformation of 4H-SiC wafers, the processing of the Si face and C face of 4H-SiC wafers can be optimized to reduce the processing damages and costs while maintaining the high quality of the 4H-SiC wafers.

Nanoindentation has been regarded as an ideal approach to investigate the mechanical properties and deformation mechanisms of semiconductors [11, 12]. By combining the nanoindentation tests and transmission electron microscope (TEM) observations, the nucleation and slip of basal plane dislocations (BPDs) are found to dominate the plastic deformation of 4H-SiC [13, 14]. The formation and propagation of cracks give rise to the brittle deformation of 4H-SiC, which is characterized by the fracture toughness [15–18]. The elastic-plastic transition of the 4H-SiC crystal was determined at a depth of $\sim$23 nm with the shear stress of 21 GPa [19–21]. It has been found that the critical depth of the crack formation is 91.7 nm for 4H-SiC [22]. In more recent studies, the nanoscale anisotropy deformation behavior of 4H-SiC have been investigated by nanoindentation [23]. It has been found that the (0001) plane has higher hardness than that of $\left(10\bar{1}0\right)$ plane. However, the anisotropic mechanical properties of Si face and C face of 4H-SiC wafers, which is mostly relevant to the mechanical wafering process, is still ambiguous.

In this work, the anisotropic mechanical properties and anisotropic deformation mechanisms of 4H-SiC wafers are systematically investigated combining nanoindentation tests, Raman spectroscopy, and scanning electron microscopy (SEM) measurements. The C face of a 4H-SiC wafer has higher hardness and lower fracture toughness than those of the Si face. The deformation of 4H-SiC is assisted by the nucleation and slip of BPDs, especially the slip of the Si-core PD of the BPDs. Therefore, the lattice-plane dependent deformation of 4H-SiC originates from different environments for the nucleation and slip of Si-core PDs. The nucleation and slip of the Si-core PD in the Si face of 4H-SiC is easier than that in the C-face, which releases the nanoindentation-induced stress and results in the decrease of the hardness and the increase of the fracture toughness of the Si face of 4H-SiC wafers. With the hexagonal lattice of 4H-SiC, the hardness along the $< 1\bar{1}00 >$ is higher than that along the $< 11\bar{2}0 >$, but the fracture toughness along the $< 1\bar{1}00 >$ is lower than that along the $< 11\bar{2}0 >$, as a result of enhanced glide of dislocations along the most closely-packed lattice direction. The insights gained in this work are expected to shed light on the optimization of the mechanical processing of 4H-SiC wafers.

2. Experimental methods

4H-SiC wafers were purchased from SICC Co., Ltd. The C face and Si face of the 4H-SiC samples were treated by CMP, with the surface roughness being less than 0.3 nm. The surface roughness of the 4H-SiC wafers were measured by atomic force microscope (AFM) (Bruker, Dimension XR) with 10×10 μm^2 scanning area. As shown in figures 1(a) and (b), the surface roughness of the C face and Si face are 0.14 nm and 0.12 nm, respectively. Nanoindentation tests were carried out by the Nanointender G200 (Agilent) with a Berkovich indenter. Series of nanoindentation tests were performed under the peak loads ranging from 50 to 500 mN. Nanoindentation tests for each load were repeated by eight times to obtain reliable data. For each test, the loading and unloading times were set to be 10 s and the holding time was 5 s. The thermal drift was maintained below $\pm$0.05 nm$\cdot$s^{-1}. The hardness and elastic modulus values were determined by the Oliver and Pharr method [24, 25]. In order to investigate the anisotropic mechanical properties of 4H-SiC wafers, the nanoindentation tests were carried out on the Si face and C face of the 4H-SiC samples (As shown in figure 1(c)). On each lattice plane, the directions of the indenter ridge were set to be parallel to the $< 1\bar{1}00 >$ and $< 11\bar{2}0 >$ of the 4H-SiC wafers, respectively (As shown in figure 1(d)). According to the planes and indenter directions, the anisotropic nanoindentation tests are referred to as Si face $< 1\bar{1}00 >$, Si face $< 11\bar{2}0 >$, C face $< 1\bar{1}00 >$ and C face $< 1\bar{1}00 >$ in this work. Confocal Raman spectroscopy was carried out using a WITec Alpha300R micro-Raman spectrometer equipped with a 75 mW green-diode laser operating at 532 nm. After each nanoindentation test, the SEM (Carl Zeiss, Gemini300) was immediately employed to characterize the lengths of the cracks of the nanoindentated 4H-SiC sample to avoid the spring back behavior.

3. Results and discussion

Figures 2(a) and (b) shows the typical load-displacement (*P*-*h*) curves of the C face and Si face of 4H-SiC under peak loads ranging from 50 to 500 mN. In these cases, the indenters are oriented along $< 11\bar{2}0 >$. Under the load of 500 mN, pop-in events occur in both the C face and Si face of the 4H-SiC wafer. Because the pop-in events occur at the high load of 500 mN, the formation and propagation of cracks or micro cracks could be the origin of the pop-in events [26]. It is clear the maximum indentation depth of the C face is larger than that of the Si face under the same load, indicating that the C face has higher hardness than the Si face of 4H-SiC.

To clarify the anisotropic deformation of 4H-SiC along different lattice orientations, we then investigate the effect of the direction of the indenter on the mechanical properties of

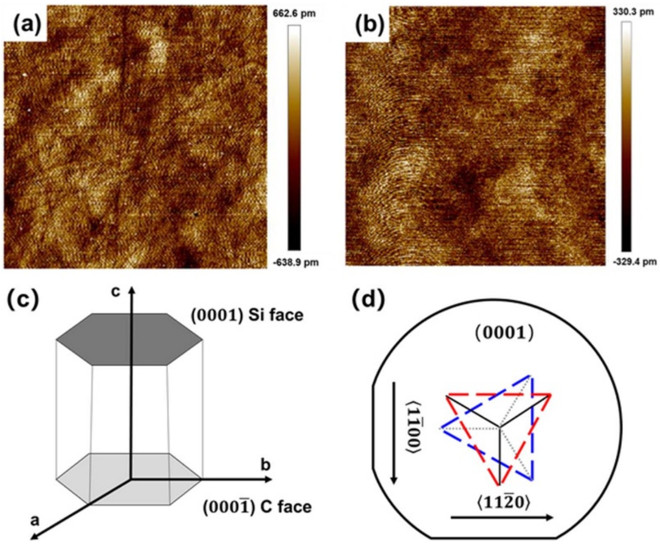

Figure 1. AFM images of (a) C face and (b) Si face of a 4H-SiC wafer. Schematic diagram of (c) C face and Si face of 4H-SiC and (d) the definition of indenter orientations. The blue and red triangles indicate the indenter orientations along $< 11\bar{2}0 >$ and $< 1\bar{1}00 >$, respectively.

4H-SiC. Taking the nanoindentation at the Si face of 4H-SiC as an example, the *P-h* curves of nanoindentated 4H-SiC along $< 1\bar{1}00 >$ and $< 11\bar{2}0 >$ are shown in figures 2(b) and (c). It turns out that the maximum indentation depth along $< 11\bar{2}0 >$ is higher than that along $< 1\bar{1}00 >$, suggesting that the hardness of 4H-SiC along $< 1\bar{1}00 >$ is higher than that along $< 11\bar{2}0 >$.

The measured values of the hardness of the C face and Si face of 4H-SiC as functions of the peak loads are displayed in figure 3(a). Due to the influence of unintentional scratches, pits, bumps and subsurface damages of the sample, the single nanoindentation result may be different to other, resulting in the high standard deviation of hardness and modulus. The values of the hardness of both the C face and Si face of 4H-SiC decrease with the increase of the peak load. This is attributed to the indentation size effect (ISE), which originates from the burst of dislocations during the loading process [27, 28]. In the non-ISE region, the values of the hardness of the C face and Si face are 37.0 ± 0.3 GPa and 35.0 ± 0.2 GPa, respectively. These values agree well with those reported in the literature [19, 21, 23]. It turns out that the hardness of the C face is higher than that of the Si face, which suggests that BPDs in the C face of 4H-SiC are more difficult to slip and the BPDs tend to pile up once they are generated. The mechanical properties along different direction of the indenter are also exhibited in figure 3(b) and figure 3(d). As shown in figure 3(b), the values of the hardness of 4H-SiC along $< 1\bar{1}00 >$ and $< 11\bar{2}0 >$ also decrease with the increase of the peak load, as a result of the ISE effect. It is clear that the hardness of 4H-SiC along the $< 1\bar{1}00 >$ is higher than that along the $< 11\bar{2}0 >$. The lattice-orientation dependent hardness is attributed to the nature of the active slip system of 4H-SiC. Because atoms are more closely packed along the $< 11\bar{2}0 >$, the slip of dislocations in the slip

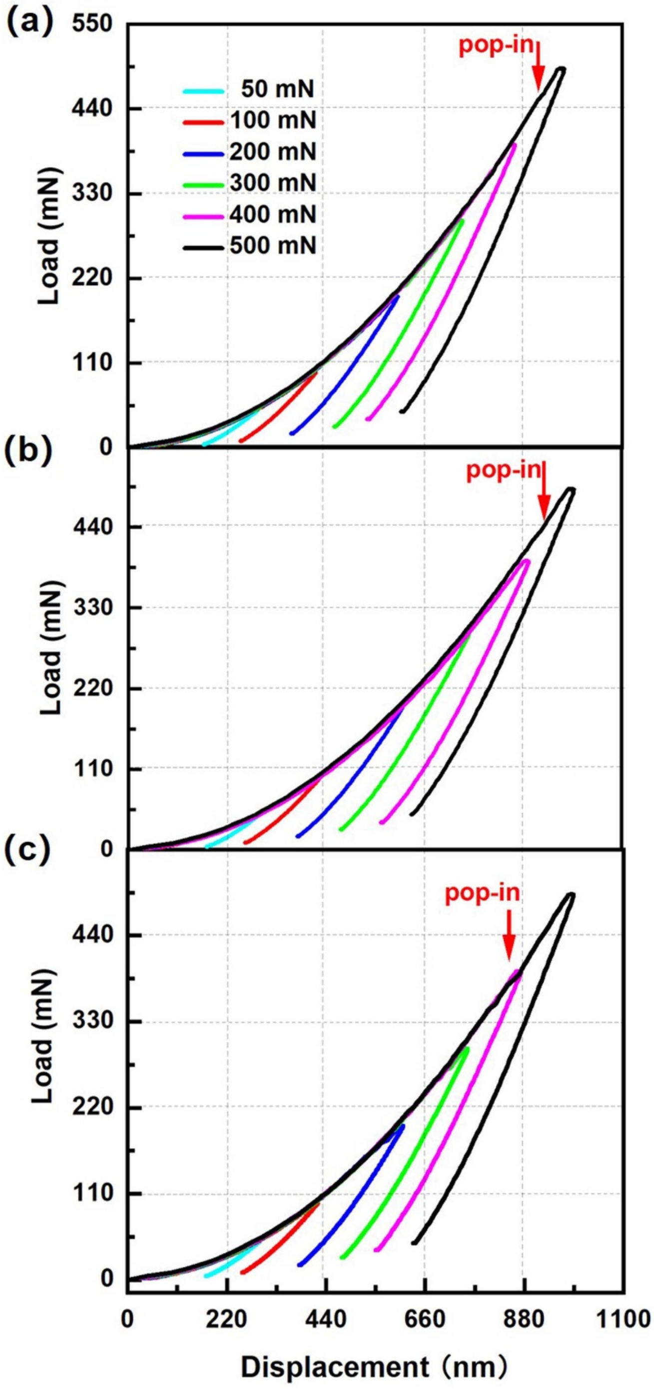

Figure 2. *P-h* curves for (a) C face $< 11\bar{2}0 >$, (b) Si face $< 11\bar{2}0 >$ and (c) Si face $< 1\bar{1}00 >$ of the 4H-SiC wafer at various maxmium load from 50 to 500 mN.

system of the (0001) $< 11\bar{2}0 >$ requires lower stress compared to that in the slip system of the (0001) $< 1\bar{1}00 >$ under the same peak load [29]. This gives rise to the lower hardness of 4H-SiC along $< 11\bar{2}0 >$.

As shown in figure 3(c), the values of the elastic modulus of both the C face and Si face of the 4H-SiC wafer decrease with the increase of the indentation load. The possible reason for the load-dependence of the elastic modulus may be attributed to

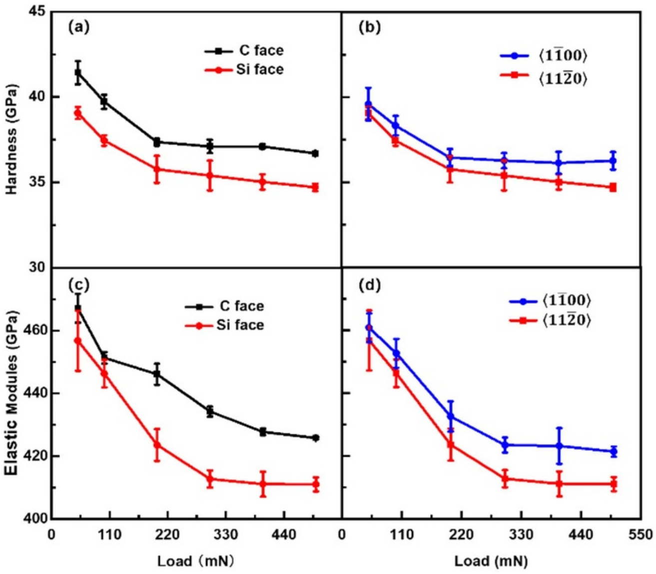

Figure 3. Values of hardness for (a) the C face and Si face of 4H-SiC along $< 11\bar{2}0 >$, and (b) those of the Si face along $< 11\bar{2}0 >$ and $< 1\bar{1}00 >$. Values of elastic modulus for (c) the C face and Si face of 4H-SiC along $< 11\bar{2}0 >$, and (d) those of the Si face along $< 11\bar{2}0 >$ and $< 1\bar{1}00 >$. The values of hardness and elastic modulus are calculated by the average value of the eight times of nanoindentation results.

the combined effect of the surface roughness, tip roundness, and the tip area [30]. As the indentation load increases to 400 mN, the elastic modulus of the C face and Si face of 4H-SiC reaches the saturation values of 426 $\pm$ 0.1 GPa and 411 $\pm$ 0.1 GPa, respectively, which are consistent with previous results [28, 31]. It is clear that the elastic modulus of the C face is higher than that of the Si face of the 4H-SiC wafer. The elastic modulus of 4H-SiC is related to the ability of the crystal to resist deformations, which dependents on the nucleation and slip of dislocations [20]. In 4H-SiC, the slip of the Si-core PDs dominates the slip of nanoindentation-induced BPDs. The nucleation and slip of the Si-core PDs at the Si face is easier than those at the C face of 4H-SiC, which lowers the elastic modulus of the Si face. Figure 3(d) shows the values of elastic modulus of 4H-SiC as functions of the peak load along the $< 11\bar{2}0 >$ and $< 1\bar{1}00 >$. The elastic modulus of 4H-SiC along $< 1\bar{1}00 >$ is larger than that along $< 11\bar{2}0 >$. Besides the slip of dislocations, the elastic modulus of a crystal is also correlated with the elastic potential energy, which depends on the number and the bonding energy of broken bonds during the slip of dislocations. Because there exist more broken bonds along the $< 1\bar{1}00 >$, higher energy is required to initiate the slip of dislocations along the $< 1\bar{1}00 >$. Therefore, the elastic modulus of 4H-SiC along the $< 1\bar{1}00 >$ is higher than that along the $< 1\bar{1}00 >$.

The hardness anisotropy and elastic-mudulus anisotropy are defined as the ratio of that along the $< 11\bar{2}0 >$ and $< 1\bar{1}00 >$. Figure 4(a) displays the variations of the hardness anisotropy as functions of the indentation load. Both orientations exhibited hardness anisotropy. However, the Si face exhibited a higher hardness anisotropy. The hardness anisotropy originated from the different dislocation slip system of 4H-SiC. On the Si face, the shear stress could be easily released through the Si-core dislocation slip, resulting in perminent hardness anisotropy. In contrast, the dislocations on the C face are difficult to slip; thus, the hardness along different crystal orientations are basically the same. Therefore, the slip of the Si-core dislocations lead to higher hardness anisotropy of the Si face. Figure 4(b) shows the elastic modulus anisotropy for C face and Si face of 4H-SiC wafers. Both Si face and C face exhibited elastic-modulus anisotropy. Moreover, the elastic-modulus anisotropy (figure 4(b)) of Si face and C face shows no significant difference as the error bars are larger than the elastic anisotropy difference.

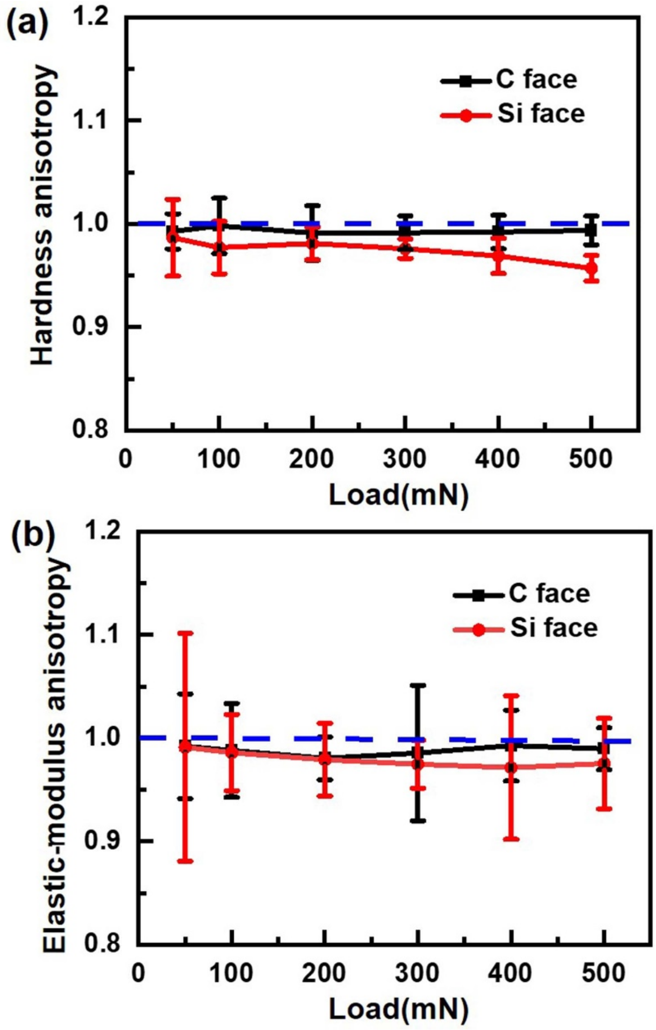

Figure 4. Variations in (a) hardness anisotropy and (b) elastic-modulus anisotropy of the Si face and C face of 4H-SiC.

The micro-Raman spectra are then measured to characterize the deformation mechanism of 4H-SiC. As shown in figure 5, the Raman spectra is measured at the nanoindentated C face, nanoindentated Si face and the pristine surface of 4H-SiC. It shows that all the Raman peak positions are found for both the pristine and nanoindentated 4H-SiC, which located at 204 cm^{-1} (FTA mode), 776 cm^{-1} (FTO mode) and 796 cm^{-1} (FTO mode) and 964 cm^{-1} (FLO mode),

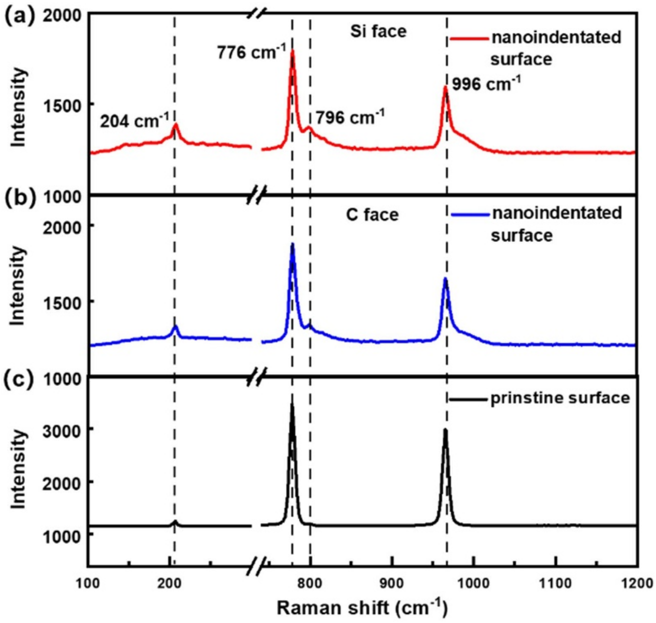

Figure 5. Raman spectra obtained for the nanoindentated (a) C face, (b) Si face and (c) the pristine surface of 4H-SiC.

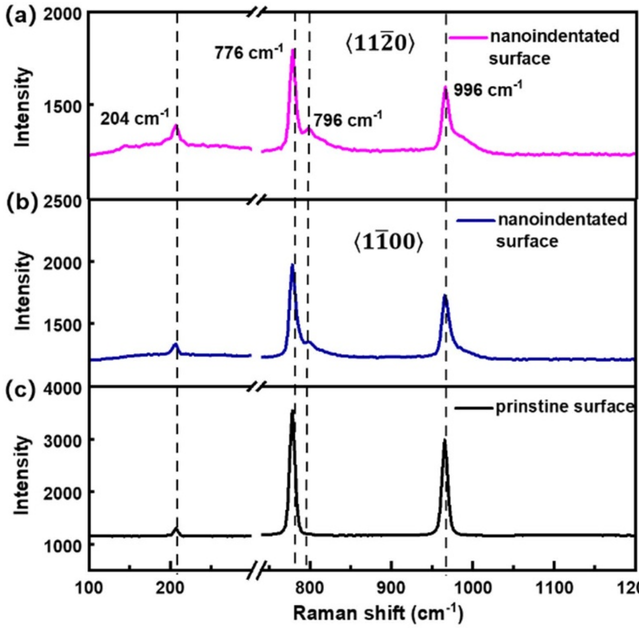

Figure 6. Raman spectra obtained for the nanoindentated Si surfaces of 4H-SiC along (a) $< 11\bar{2}0 >$, (b) $< 1\bar{1}00 >$ and (c) the pristine Si surface.

matching well with the Raman spectra of 4H-SiC [32, 33]. We find that the peak of the FTA mode broadens for the nanoindentated C face and Si face of 4H-SiC, as a result of lattice distortions caused by formation of dislocations. The broadening of the FTA peak of the nanoindentated Si face is more severe than that of the C face, which indicates that the amount of nanoindentation-induced dislocations and thus the lattice distortion is more prominent for the nanoindentated Si face of 4H-SiC.

As shown in figure 6, the micro-Raman spectra for 4H-SiC along $< 11\bar{2}0 >$ and $< 1\bar{1}00 >$ are adopted to characterize the lattice-orientation dependent deformation of 4H-SiC wafers. The FTA (204 cm^{-1}), FTO (776 cm^{-1} and 796 cm^{-1}), and FLO (996 cm^{-1}) modes are found at the nanoindentated surface of 4H-SiC. It is found the broadening of the FTA mode for the nanoindentated surface along $< 11\bar{2}0 >$ is more severe than that long $< 1\bar{1}00 >$, suggesting that the lattice distortions caused by the dislocation slip along $< 11\bar{2}0 >$ is more severe than that along $< 1\bar{1}00 >$. This is consistent with the nanoindentation measurement results, which suggested that the dislocations along $< 11\bar{2}0 >$ could slip more easily than those along $< 1\bar{1}00 >$; thus, the hardness of $< 11\bar{2}0 >$ is lower than $< 1\bar{1}00 >$. Of note, the intensity of the FTO mode located at 796 cm^{-1} increases after nanoindentation, which is correlated with severe lattice distortions or phase transitions. The relative variations in FTO (796 cm^{-1}) and FTA (204 cm^{-1}) have been commonly used to distinguish whether phase transition has occurred. As tabulated in table 1, the ratio $r\left(\frac{\mathrm{FTO}}{\mathrm{FTA}}\right)$ is unchanged for the nanoindentated C face and Si face in the $< 1\bar{1}00 >$ and $< 11\bar{2}0 >$. This indicates that the phase transition of 4H-SiC did not occur in nanoindentated 4H-SiC.

Figure 7 shows a typical SEM images of the indenter prints for Si face $< 1\bar{1}00 >$, Si face $< 11\bar{2}0 >$, C face $< 1\bar{1}00 >$ and C face $< 1\bar{1}00 >$ of 4H-SiC. As shown in the figure 7(a), all cracks are well- developed ($c > 2a$), where a is the size of the indenter print from the center to the corner, l is the crack length from the indented corner to the crack tip, and c is the crack length ($c = a + l$). The crack length c of the indent was determined by [34]:

$$c = \frac{1}{3}(c_1 + c_2 + c_3) \tag{1}$$

where the definitions of c_1, c_2, and c_3 are illustrated in figure 7(a). The values of a and l were also defined using the same approach. As shown in figure 7, no lateral cracks were observed. It should be noted that the lateral cracks could potentially affect the plastic deformation zone and influence radial crack length. Therefore, nanoindentation without lateral cracks could be used to compare the fracture toughness of 4H-SiC. As shown in figure 8, the crack lengths for the C face were longer than that for Si face, suggesting that the cracks in the C face formed and propagated more easily than in the Si face. The average crack length of nanoindentated 4H-SiC with a load of 500 mN is plotted in figure 8. The crack length for nanoindentated 4H-SiC decreased in the order of C face $< 1\bar{1}00 >$, C face $< 11\bar{2}0 >$, Si face $< 11\bar{2}0 >$ and Si face $< 1\bar{1}00 >$.

Considering that the crack length is inversely proportional to the fracture toughness, we speculated that the fracture toughness increased in the order of C face $< 1\bar{1}00 >$, C face $< 11\bar{2}0 >$, Si face $< 11\bar{2}0 >$ and Si face $< 1\bar{1}00 >$.

The fraction toughness ($\mathrm{K_{IC}}$) of 4H-SiC is then calculated by [34]:

$$K_{IC} = A\left(\frac{a}{l}\right)^{\frac{1}{2}}\left(\frac{E}{H}\right)^{\frac{2}{3}}\frac{P}{c^{2/3}} \tag{2}$$

Table 1. Summary of Raman intensities for FTO mode (796 cm^{-1}), FTA mode (204 cm^{-1}), as well as their ratio $r\left(\frac{FTO}{FTA}\right)$ on the pristine surface, as well as the nanoindentated Si face $<1\bar{1}00>$, Si face $<11\bar{2}0>$, C face $<1\bar{1}00>$ and C face $<1\bar{1}00>$ of 4H-SiC.

			796 cm^{-1}	204 cm^{-1}	$r\left(\frac{FTO}{FTA}\right)$
Si face	$<1\bar{1}00>$	Pristine surface		1343	
		Nanoindentated surface	1379	1324	1.04
	$<11\bar{2}0>$	Pristine surface		1343	
		Nanoindentated surface	1351	1318	1.03
C face	$<1\bar{1}00>$	Pristine surface		1300	
		Nanoindentated surface	1343	1332	1.00
	$<11\bar{2}0>$	Pristine surface		1340	
		Nanoindentated surface	1305	1326	0.98

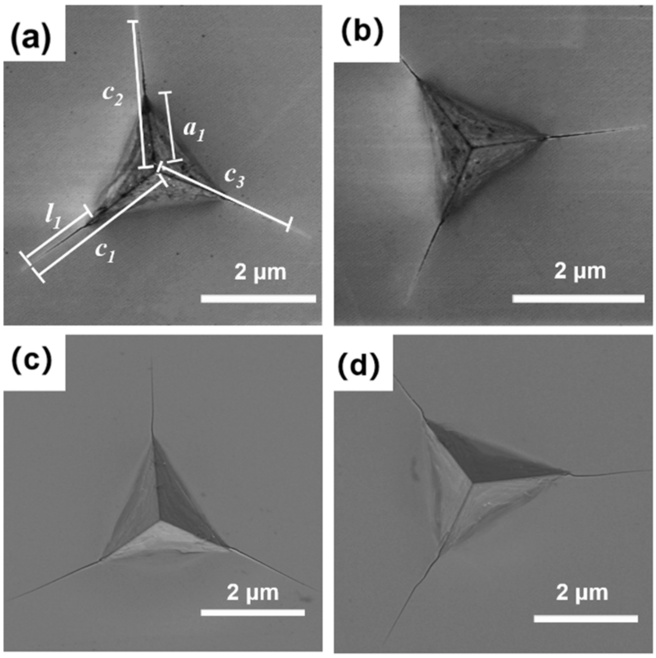

Figure 7. Typical SEM images of nanoindentated 4H-SiC under a peak load of 500 mN: (a) Si face $<11\bar{2}0>$, (b) Si face $<1\bar{1}00>$, (c) C face $<11\bar{2}0>$ and (d) C face $<1\bar{1}00>$, where the dimension of *c*, *l* and *a* are illustrated in figure 7 (a).

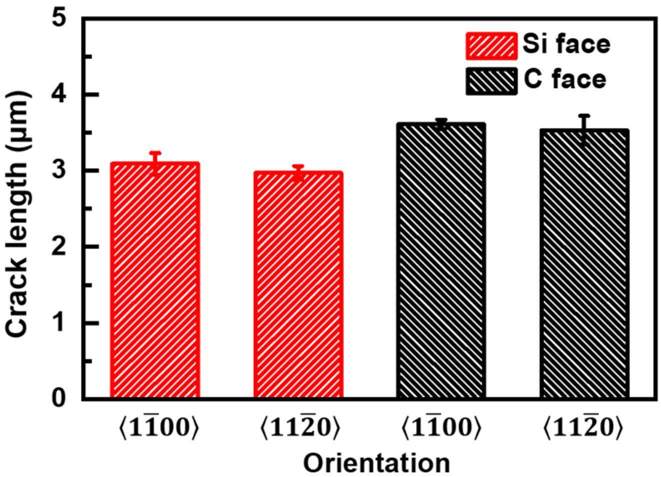

Figure 8. Average crack length for the nanoindentated 4H-SiC along different orientations at the Si face and C face of 4H-SiC under the load of 500 mN. The error bars represent the standard deviation.

where P is the applied load, A is a constant that relates to the indenter geometry (Berkovich indenter used in this study, $A = 0.0016$), and E and H denote the elastic modulus and hardness of 4H-SiC, respectively. We derive the fracture toughness using ten nanoindentation tests without lateral cracks. As shown in table 2, the calculated fracture toughness increased in order of C face $<1\bar{1}00>$, C face $<11\bar{2}0>$, Si face $<11\bar{2}0>$, Si face $<1\bar{1}00>$, which is consistent with the conclusions show in figure 7. The fracture toughness for the Si face and C face are 3.81 ± 0.02 $MPa \cdot m^{\frac{1}{2}}$ and 2.94 ± 0.02 $MPa \cdot m^{\frac{1}{2}}$, respectively. This is consistent with the values previously reported [23]. It has been widely recognized that fracture toughness is correlated with surface energy and dislocations. As previously mentioned, the Si-core dislocations in the Si face can easily slip and releases the shear stress induced by nanoindentation. In contrast, the C face hinders the slip of dislocations and accumulated a high-stress field at the C face, which facilitates the formation of cracks in the C face. In addition, it has been previously reported that the surface energy of the Si face is higher than that of the C face. The lower surface energy of the C face make it easier for cracks to form in the C face of 4H-SiC. Therefore, the C face was believed to have a higher fracture toughness than the Si face.

At last, we discuss effect of anisotropic deformation on the mechanical processing of 4H-SiC substrate wafers. The C face of 4H-SiC wafers has higher hardness and lower fracture toughness than those of the Si face. Under the same processing parameters during the wire slicing of 4H-SiC, the amount of processing-induced dislocations and surface damages of the C face is higher than that of the Si face of 4H-SiC, which agree with the study reported by Yao *et al* [35]. The lattice-orientation dependent deformation may provide clue to optimization of the feed direction of the wire during the wiresawing of 4H-SiC wafers. In addition, the flatness of 4H-SiC wafers might be optimized by tuning the sequence of lapping due to the different surface-damage thickness of the C face and Si face of 4H-SiC wafers. During the lapping of sliced 4H-SiC wafers, the material removal thicknesses of the Si face and C

Table 2. Average crack lengths, values of E/H and fracture toughness (K_{IC}) for the Si face $< 11\bar{2}0 >$, Si face $< 1\bar{1}00 >$, C face $< 11\bar{2}0 >$ and C face $< 1\bar{1}00 >$.

		Crack length (μm)	E/H	K_{IC}
Si face	$< 1\bar{1}00 >$	2.97 ± 0.19	13.58 ± 0.13	3.81 ± 0.02
	$< 11\bar{2}0 >$	3.09 ± 0.06	13.78 ± 0.25	3.62 ± 0.01
C face	$< 1\bar{1}00 >$	3.53 ± 0.24	13.56 ± 0.35	2.94 ± 0.02
	$< 11\bar{2}0 >$	3.61 ± 0.14	13.75 ± 0.67	1.87 ± 0.03

face are the same. In order to optimize the processing parameters of 4H-SiC wafers and decrease the costs of 4H-SiC wafers, the removal-material thickness of the C face can be decreased. On the other hand, during the lapping of 4H-SiC wafers, the machining stress for the Si face can be lower than that for C face.

4. Conclusions

In conclusion, we have systematically investigated the anisotropic deformation of 4H-SiC and found that the hardness and elastic modulus values of the C face were higher than the Si face. The fracture toughness of the C face was lower than that for Si face. The anisotropic deformation mechanism of 4H-SiC resulted from the nucleation and slip mechanisms of the dislocations. The Si-core dislocations in the Si face is easier to slip and nucleation than those in the C face, resulting in the lower hardness and higher fracture toughness of the Si face. In contrast, the C-core dislocations in the C face were difficult to slip, which accumulates high stresses in the C face and reduces the fracture toughness of 4H-SiC. The hardness of 4H-SiC along $< 1\bar{1}00 >$ is higher than that of $< 11\bar{2}0 >$ and the fracture toughness along $< 1\bar{1}00 >$ is lower than that of $< 11\bar{2}0 >$, as a result of enhanced glide of dislocations along the most closely packed direction. The insights gained in this work are expected to shed light on the optimization of the mechanical processing of 4H-SiC wafers.

Data availability statement

The data generated and/or analysed during the current study are not publicly available for legal/ethical reasons but are available from the corresponding author on reasonable request.

Acknowledgments

This work is supported by 'Pioneer' and 'Leading Goose' R&D Program of Zhejiang (Grant No. 2022C01021), National Key Research and Development Program of China (Grant No. 2018YFB2200101), Natural Science Foundation of China (Grant Nos. 91964107, 61774133), Fundamental Research Funds for the Central Universities (Grant No. 2018XZZX003-02), Natural Science Foundation of China for Innovative Research Groups (Grant No. 61721005) and Zhejiang University Education Foundation Global Partnership Fund.

ORCID iDs

Rong Wang https://orcid.org/0000-0003-3333-0180
Xiaodong Pi https://orcid.org/0000-0002-4233-6181

References

[1] Abe Y, Chaen A, Sometani M, Harada S, Yamazaki Y, Ohshima T and Umeda T 2022 Electrical detection of T_{V2a}-type silicon vacancy spin defect in 4H-SiC MOSFETs *Appl. Phys. Lett.* **120** 064001
[2] Kleppinger J W, Chaudhuri S K, Karadavut O and Mandal K C 2021 Role of deep levels and barrier height lowering in current-flow mechanism in 150 μm thick epitaxial n-type 4H-SiC Schottky barrier radiation detectors *Appl. Phys. Lett.* **119** 063502
[3] Wang F *et al* 2020 Coherent control of nitrogen-vacancy center spins in silicon carbide at room temperature *Phys. Rev. Lett.* **124** 223601
[4] Cha K and Kim K 2021 3.3 kV 4H-SiC DMOSFET with a source-contacted dummy gate for high-frequency applications *J. Semicond.* **42** 062801
[5] Luo X, Zhang K, Song X, Fang J, Yang F and Zhang B 2020 4H-SiC trench MOSFET with an integrated Schottky barrier diode and L- shaped P+ shielding region *J. Semicond.* **41** 102801
[6] Lim S G, Jackson T N, Mitchel W C, Bertke R and Freeouf J L 2001 Optical characterization of 4H-SiC by far ultraviolet spectroscopic ellipsometry *Appl. Phys. Lett.* **79** 162
[7] Lu J, Luo Q, Xu X, Huang H and Jiang F 2019 Removal mechanism of 4H-and 6H-SiC substrates (0001 and 0001 over bar) in mechanical planarization machining *Proc. Inst. Mech. Eng.* B **233** 69
[8] Yan J, Gai X and Harada H 2010 Subsurface damage of single crystalline silicon carbide in nanoindentation tests *J. Nanosci. Nanotechnol.* **10** 7808
[9] Tian Z, Chen X and Xu X 2020 Molecular dynamics simulation of the material removal in the scratching of 4H-SiC and 6H-SiC substrates *Int. J. Extreme Manuf.* **2** 045104
[10] Chen X-F, Xu X-G, Hu X-B, Li J, Jiang S-Z, Ning L-N, Wang Y-M and Jiang M-H 2007 Anisotropy of chemical mechanical polishing in silicon carbide substrates *Mater. Sci. Eng.* B **142** 28
[11] Chen B, Wang J, Zhu Y, Liao X, Lu C, Mai Y-W, Ringer S P, Ke F and Shen Y 2014 Deformation-induced phase transformation in 4H-SiC nanopillars *Acta Mater.* **80** 392
[12] Wu Z, Liu W, Zhang L and Lim S 2020 Amorphization and dislocation evolution mechanisms of single crystalline 6H-SiC *Acta Mater.* **182** 60
[13] Liu X, Zhang J, Xu B, Lu Y, Zhang Y, Wang R, Yang D and Pi X 2022 Deformation of 4H-SiC: the role of dopants *Appl. Phys. Lett.* **120** 052105
[14] Guo J, Ailihumaer T, Peng H, Raghothamachar B and Dudley M 2018 *In-situ* synchrotron x-ray topography study

on the stress relaxation process in 4H-SiC homoepitaxial layers, in: symposium on gallium nitride and silicon carbide power technologies *ECS Trans.* **86** 75

[15] Li Z, Ghosh A, Kobayashi A S and Bradt R C 1989 Indentation fracture-toughness of sintered silicon-carbide in the palmqvist crack regime *J. Am. Ceram. Soc.* **72** 904

[16] Srinivasan S and Scattergood R O 1991 Indentation fracture-toughness of sintered silicon-carbide in the palmqvist crack regime—comment *J. Am. Ceram. Soc.* **74** 887

[17] Kunka C, Trachet A and Subhash G 2015 Interaction of indentation-induced cracks on single-crystal silicon carbide *J. Am. Ceram. Soc.* **98** 1891

[18] Malik R and Kim Y-W 2022 Effects of initial alpha-phase content on properties of pressureless solid-state sintered SiC ceramics *Int. J. Appl. Ceram.* **19** 703

[19] Wasmer K, Ballif C, Gassilloud R, Pouvreau C, Rabe R, Michler J, Breguet J M, Solletti J M, Karimi A and Schulz D 2005 Cleavage fracture of brittle semiconductors from the nanometer to the centimeter scale *Adv. Eng. Mater.* **7** 309

[20] Goel S, Yan J, Luo X and Agrawal A 2014 Incipient plasticity in 4H-SiC during quasistatic nanoindentation *J. Mech. Behav. Biomed.* **34** 330

[21] Nawaz A, Mao W G, Lu C and Shen Y G 2017 Nano-scale elastic-plastic properties and indentation-induced deformation of single crystal 4H-SiC *J. Mech. Behav. Biomed. Mater.* **66** 172

[22] Chai P, Li S and Li Y 2019 Modeling and experiment of the critical depth of cut at the ductile-brittle transition for a 4H-SiC single crystal *Micromachines* **382** 10

[23] Prasad K E and Ramesh K T 2019 Hardness and mechanical anisotropy of hexagonal SiC single crystal polytypes *J. Alloys Compd.* **770** 158

[24] Oliver W C and Pharr G M 1992 An improved technique for determining hardness and elastic-modulus using load and displacement sensing indentation experiments *J. Mater. Res.* **7** 1564

[25] Oliver W C and Pharr G M 2004 Measurement of hardness and elastic modulus by instrumented indentation: advances in understanding and refinements to methodology *J. Mater. Res.* **19** 3

[26] Matsumoto M, Huang H, Harada H, Kakimoto K and Yan J 2017 On the phase transformation of single-crystal 4H-SiC during nanoindentation *J. Phys. D: Appl. Phys.* **50** 265303

[27] Zhu P, Zhao Y, Agarwal S, Henry J and Zinkle S J 2022 Toward accurate evaluation of bulk hardness from nanoindentation testing at low indent depths *Mater. Des.* **213** 110317

[28] Nix W D and Gao H J 1998 Indentation size effects in crystalline materials: a law for strain gradient plasticity *J. Mech. Phys. Solids* **46** 411

[29] Niihara K 1979 Slip systems and plastic-deformation of silicon-carbide single-crystals at high-temperatures *J. Less-Common Met.* **65** 155

[30] Chen L, Ahadi A, Zhou J and Stahl J-E Modeling effect of surface roughness on nanoindentation tests *14th CIRP 2013 Conf. on Modeling of Machining Operations* p 334

[31] Ning X J, Huvey N and Pirouz P 1997 Dislocation cores and hardness polarity of 4H-SiC *J. Am. Ceram. Soc.* **80** 1645

[32] Yang J, Song H, Jian J, Wang W and Chen X 2021 Characterization of morphological defects related to micropipes in 4H-SiC thick homoepitaxial layers *J. Cryst. Growth* **568** 126182

[33] Mahadik N A *et al* 2011 Structure and morphology of inclusions in 4 degrees offcut 4H-SiC epitaxial layers *J. Electron. Mater.* **40** 413

[34] Schiffmann K I 2011 Determination of fracture toughness of bulk materials and thin films by nanoindentation: comparison of different models *Phil. Mag. Lett.* **91** 1163

[35] Yao Y Z, Ishikawa Y, Sugawara Y and Sato K 2015 Removal of mechanical-polishing-induced surface damages on 4H-SiC by chemical etching and its effect on subsequent epitaxial growth *Mater. Sci. Forum* **821–823** 541–4